Giannopoulos *et al. Biochar* (2026) 8:130
https://doi.org/10.1007/s42773-026-00648-2

Biochar

ORIGINAL RESEARCH Open Access

Sorption and transport of *Escherichia coli* CN-13 in saturated sand columns amended with biochar derived from malt spent rootlets

Christos P. Giannopoulos[1], Christos A. Kolotouros[1] and Ioannis D. Manariotis[1*]

Abstract

Pathogenic microorganism transport through sandy soils and engineered sand filtration systems represents a significant groundwater contamination risk; biochar amendment of these media offers a sustainable retention strategy. This study investigated the sorption and transport of *Escherichia coli* (*E. coli*) CN-13 in saturated sand columns amended with biochar derived from malt spent rootlets (MSRB) pyrolyzed at 850 °C. Batch experiments were conducted to quantify inactivation and adsorption kinetics under varying ionic strengths (1 and 150 mM KCl). *E. coli* inactivation was best described by the Weibull model, while adsorption kinetics and isotherms followed the pseudo-first-order (PFO) and Freundlich models, respectively. Increasing ionic strength was found to hinder adsorption capacity, likely due to electrostatic shielding and increased competition for active sorption sites. Column transport experiments demonstrated that amending sand with MSRB significantly enhanced bacterial retention, with removal efficiencies increasing from 17.8% in unamended sand to 94.1% in sand containing 10% (w/w) biochar. Numerical modeling using the one-dimensional biocolloid transport equation (1D-BTE) revealed that while physical straining dominated removal in unamended and 5% biochar columns, direct attachment became the governing mechanism at 10% biochar application rate. The attachment of bacteria to MSRB was found to be irreversible. These results indicate that MSRB is a promising low-cost amendment for enhancing pathogen retention in sandy porous media, with direct relevance to engineered sand filtration and applications in agricultural sandy soils, while simultaneously addressing brewery waste disposal challenges.

Highlights

- Sand with 10% malt spent rootlets biochar achieved 94.1% *E. coli* removal.
- Biochar shifted *E. coli* retention mechanism from physical straining to direct attachment.
- *E. coli* sorption was irreversible, following pseudo-first-order kinetics and Freundlich isotherm behavior.

Keywords Biochar, Malt spent rootlets, *E. coli*, Sand filtration, Adsorption kinetics

*Correspondence:
Ioannis D. Manariotis
idman@upatras.gr
Full list of author information is available at the end of the article

Springer

Graphical Abstract

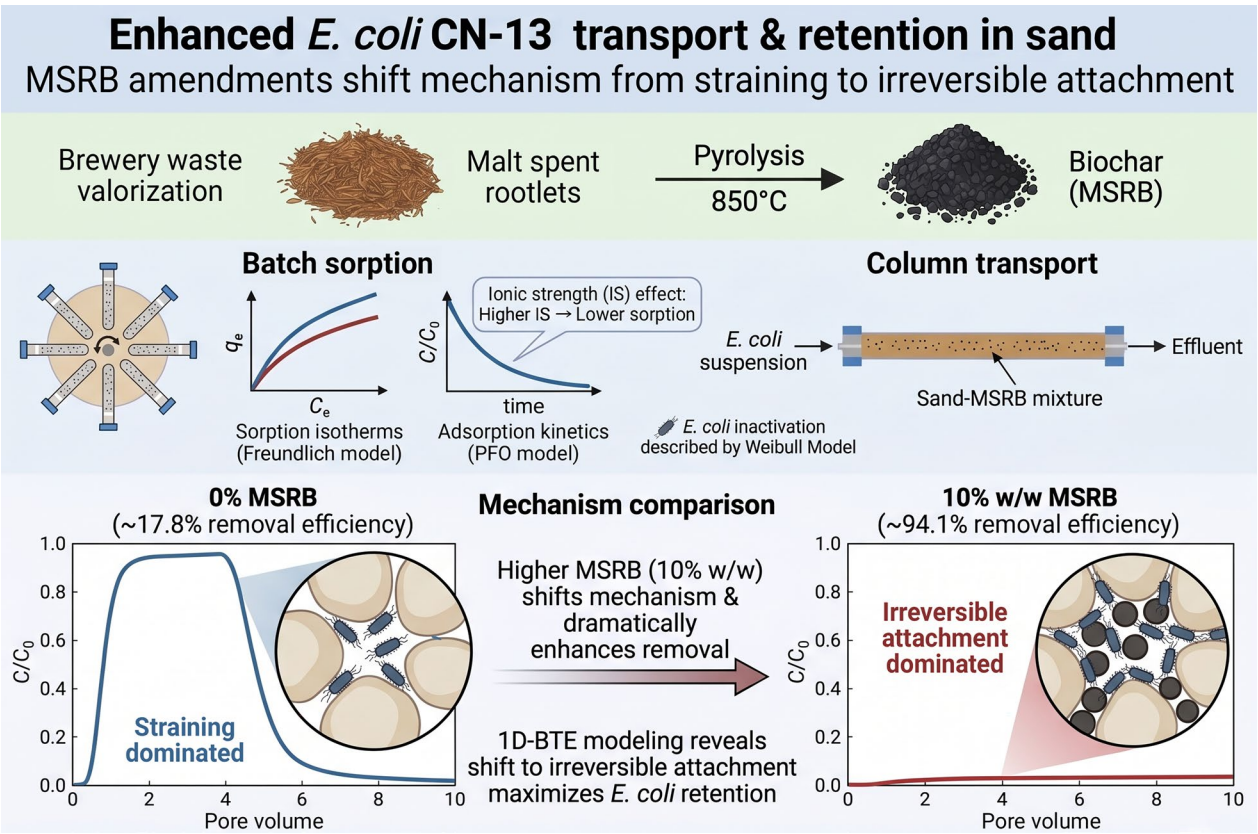

1 Introduction

The application of animal or human fecal materials to soil for agricultural purposes and their downward percolation through the vadose zone via irrigation or precipitation events toward aquifers result in groundwater contamination, which constitutes a worldwide public health concern (Bagordo et al. 2024). Historical evidence shows that numerous epidemic outbreaks have been attributed to waterborne pathogenic microorganisms derived from fecal contamination of groundwater, with an estimated one million people dying annually from diarrheal diseases linked to poor sanitation and unsafe water in domestic settings (Wolf et al. 2023). The fate and transport of pathogenic microorganisms in subsurface environments are governed by a complex interplay of physicochemical processes that depend on soil properties, including soil structure, texture, water saturation, ionic strength, pore-size distribution, surface charge, and organic carbon content (Masciopinto and Fadakar Alghalandis 2023; Singer et al. 2025).

Biochar, defined as the charred organic matter produced through pyrolysis of biomass under oxygen-limited conditions, has emerged as a promising and sustainable sand filtration system amendment for mitigating the transport of pathogens. The application of biochar to soil affects microorganism mobility through modification of the physicochemical properties of the soil matrix and enhancing direct sorption and retention of microorganisms owing to the biochar's high specific surface area (SSA) (Zeng and Kan 2023). Beyond the biochar's role in pathogen mitigation, its high carbon content and chemical stability have generated considerable interest in its use for atmospheric carbon sequestration (Lehmann et al. 2006) and the reduction of greenhouse gas emissions (Jha et al. 2010). Biochar amendments have been increasingly adopted in agriculture because of their dual environmental and agronomic benefits associated with improved soil fertility and crop productivity resulting from increased soil water-holding capacity, enhanced nutrient availability, improved soil structure, and increased cation exchange capacity (Jia et al. 2023; Li et al. 2024).

Despite the growing body of research on biochar's capacity to retain nutrients, heavy metals, and pesticides in soil, knowledge remains limited regarding how biochar affects microbial transport behavior in saturated porous media and the relative contribution of the underlying physicochemical mechanisms governing these interactions. The available literature on biochar-microorganism interactions converges on several key findings regarding the factors controlling biochar's effectiveness in retaining bacterial cells. The pyrolysis temperature at which biochar is produced and the associated pyrolysis duration represent critical determinants of its bacterial removal capacity, as they affect the biochar's SSA, physicochemical properties, pore structure morphology, and surface functional groups (García-Ávila et al. 2023). Biochar produced at elevated temperatures (700–800 °C) and/or through slow pyrolysis is typically characterized by increased SSA compared to biochar produced at lower temperatures and/or through fast pyrolysis procedures (Abit et al. 2012, 2014; Bolster and Abit 2012; Bui et al. 2024; Kazemi Shariat Panahi et al. 2020; Manariotis et al. 2015). The feedstock type also influences bacterial retention capacity, with animal-based biochars generally exhibiting superior bacterial removal compared to plant-derived biochars, likely due to differences in initial biomass composition, lignin content, and thermal decomposition pathways (Downie et al. 2012).

Bolster (2019) studied the bacterial retention in sand filters amended with biochar derived from pine softwood and determined that biochar addition can enhance bacterial retention by up to 5 orders of magnitude through the direct attachment mechanism, but results vary depending on the bacterial strain and sand size. Increasing biochar concentration from 0 to 15% (v/v) had a larger impact on retention of the more hydrophobic bacteria. Similarly, Abit et al. (2012) and Bolster and Abit (2012) reported that application of biochar derived from poultry litter and pine chips at rates of 2% to 10% (w/w) achieved substantial reductions in bacterial transport, ranging from 3 to 5 orders of magnitude. The presence of natural organic matter or compost can substantially increase bacterial mobilization by competing for sorption sites on biochar surfaces, effectively exhausting available attachment sites through interactions with dissolved organic matter (Mohanty and Boehm 2014). Soil textural properties also play a significant role, with bacteria recovery from clay or loam-textured sands being substantially lower than from fine sand, consistent with the greater bacterial retention capacity of soils with higher clay content attributed to enhanced cell adhesion to clay mineral particles (Abit et al. 2014).

Among secondary parameters examined, infiltration rate and influent cell concentration have demonstrated only minor effects on microbial mobility (Haznedaroglu et al. 2009). Importantly, changes in solution pH, ionic strength, dissolved organic matter concentrations, and phosphate levels that may result from biochar amendment have been reported to exert either negligible or minimal effects on bacterial transport behavior (Bolster and Abit 2012; Dan et al. 2021). However, ionic strength may occasionally play a significant role in bacterial transport through changes in electrostatic shielding, steric interactions, or solute competition for available sorption sites (Liu et al. 2024).

While the body of knowledge regarding biochar's effects on pathogenic microorganism transport continues to expand, significant research gaps persist. First, comprehensive investigations into the sorption dynamics of pathogenic microorganisms on biochar derived from malt spent rootlets (MSRB) remain absent: although Manariotis et al. (2015) and Boutsika et al. (2014) established the physicochemical characterization of MSRB as a sorbent for mercury and other inorganic contaminants, its efficacy as a sand filtration amendment for bacterial pathogen retention has not been evaluated. Second, most reported batch biochar adsorption studies do not account for the simultaneous natural inactivation of bacteria during the sorption contact period, introducing systematic overestimation of apparent adsorption rate constants (Suliman et al. 2017; Bolster 2019). Third, the effect of ionic strength on bacterial attachment to high-temperature biochars (> 800 °C), which are fundamentally different from low-temperature counterparts, remains poorly constrained; existing ionic strength studies have largely focused on plant-derived biochars produced below 500 °C (Bolster and Abit 2012; Dan et al. 2021). Fourth, whereas some studies have reported dominant straining or dominant attachment mechanisms in biochar-amended systems, the relative contributions of these two retention pathways have rarely been quantified (Singer et al. 2025).

Herein, we investigate the fate and transport of *Escherichia coli* (*E. coli*), the most widely used indicator organism for fecal contamination and the potential presence of pathogenic microorganisms in water (Korajkic et al. 2018; Zhu et al. 2023). The primary objectives of the present study were as follows: (1) to quantify the kinetic and equilibrium sorption behavior of *E. coli* CN-13 onto MSRB through batch sorption experiments conducted at varying initial cell concentrations and solution ionic strengths; (2) to develop and validate kinetic and isotherm models that adequately describe the simultaneous inactivation and attachment of *E. coli* onto MSRB; and (3) to quantify the fate and transport of *E. coli* through biochar-amended saturated porous media and the relative contribution of different retention mechanisms through

column transport experiments. The ionic strength conditions selected for investigation were chosen to represent both low ionic strength conditions typical of pristine groundwater environments and elevated ionic strength conditions representative of contaminated groundwater or impacted soil–water systems.

To the best of our knowledge, based on a systematic literature review of Web of Science, Scopus, and Google Scholar (search date: April 2026; terms: 'malt spent rootlets biochar' AND 'bacteria OR *E. coli* OR pathogen transport'), this is the first study to (i) investigate the sorption and transport of *E. coli* in saturated sand columns amended with MSRB; (ii) simultaneously account for *E. coli* inactivation kinetics within the batch adsorption modeling framework using a validated bacterial inactivation correction, yielding concentration-independent kinetic rate constants; and (iii) systematically quantify the relative contributions of physical straining and direct attachment in MSRB-amended columns through numerical fitting of a biocolloid transport equation. MSRB represents an abundant, low-cost brewery byproduct whose valorization as a pathogen-retention amendment addresses both environmental remediation and industrial waste management objectives.

2 Materials and methods

2.1 Bacterial stock preparation

In the present study, the *E. coli* strain CN-13 derived from strain C (ATCC® 13706™) was chosen mainly because of its resistance to nalidixic acid, that enables the use of nalidixic acid in growth media to selectively grow CN-13 while inhibiting the growth of other "wild-type" bacteria that might be present. The CN-13 strain is also classified as Biosafety Level 1, thereby generally considered safe for healthy adult humans.

For the preparation of the bacterial stock solution, the procured *E. coli* CN-13 was streaked onto tryptic soy agar (TSA) plates supplemented with nalidixic acid at a final concentration of 25 μg mL^{-1} and incubated for 24 h at 37 °C to allow colony formation. The nalidixic acid selective supplement was prepared as a stock solution at 2.5 mg mL^{-1} in 0.1 M NaOH and filter-sterilized through a 0.22 μm membrane prior to addition to autoclaved media. The following day, one isolated colony was transferred to each of five Erlenmeyer flasks, each containing 150 mL TSB supplemented with 1.5 mL of the nalidixic acid stock solution (final concentration: 25 μg mL^{-1}), and cultured for 4 h at 37 °C and 150 rpm in an incubator (INNOVA 43, New Brunswick Scientific). The bacterial solution was transferred to 50-mL Falcon tubes and centrifuged for 10 min at 10,000 rpm (model SL40R, Thermo Fisher Scientific). After centrifugation, the supernatant was discarded, and the precipitated bacteria at the bottom of the tube were collected. This process was repeated until all growth media was removed and all bacteria were collected in one tube, which was filled up to 50 mL with a 9 g L^{-1} NaCl solution in order to preserve osmotic pressure. The above solution had a concentration of ~ $8.9 \cdot 10^9$ CFU mL^{-1} and was called a stock solution. The desired initial concentration, either for batch or column experiments, was achieved by consecutive tenfold dilutions. Prior to each tenfold dilution step, all tubes were vortex-mixed (10 s, maximum speed) to disrupt bacterial aggregates and ensure homogeneous cell distribution, thereby preventing underestimation of cell concentration in the diluted aliquots.

A schematic flow diagram for the bacterial stock preparation is shown in Fig. S1. Prior to the experiments, every batch of *E. coli* suspension was kept at 4 °C for 24 h in order for the bacteria to adjust to the new concentration. The bacterial concentration in the effluent was quantified by the spread plate technique. In brief, 100 μL of suspension was withdrawn from each sample to prepare dilutions ranging up to 10^{-6}, depending on the experiment. The diluted effluent samples were then placed on TSA Petri plates, and the colony-forming units were counted after overnight incubation at 37 °C. Each sample was enumerated using only plates that formed 30 to 300 colonies.

2.2 Sand and biochar preparation

As filter media in column transport experiments, middle-size quartz sand was used with a diameter ranging from 0.425 to 0.6 mm (No. 30/40 sieve), with a uniformity coefficient of $C_u = 1.21$, and a bulk density of $\rho_b = 1.65$ g cm^{-3}. Sand's chemical composition, as given by the manufacturer Filcom Filterzand & Grind, was 96.2% SiO_2, 0.15% Na_2O, 0.11% CaO, 0.02% MgO, 1.75% Al_2O_3, 0.78% K_2O, 0.06% SO_3, 0.46% Fe_2O_3, 0.03% P_2O_5, 0.02% BaO, and 0.01% Mn_3O_4. Surface impurities were removed by hydration with deionized water (DIW) for several days, drying for 24 h at 105 °C, treatment with 0.1 M NaOH for 3 h, washing up to pH 7, and repetition with 0.1 M HNO_3. The sequential cleaning procedure serves three purposes: (1) DIW hydration removes loosely bound surface fines, pre-adsorbed inorganic salts, and soluble organic residues that would alter ionic strength conditions and introduce uncontrolled carbon or nutrient loading; (2) treatment with 0.1 M NaOH dissolves organic surface coatings (humic substances, lipid films) that would introduce uncontrolled sorption sites for *E. coli*; washing to pH 7 removes residual NaOH; (3) treatment with 0.1 M HNO_3 dissolves iron and aluminum oxyhydroxide films from quartz surfaces; these oxide coatings carry a positive surface charge at near-neutral pH (PZC ~ 7–9) and would non-reproducibly enhance *E. coli*–sand attachment, possibly confounding the attribution of retention

to MSRB. The procedure produces a reproducible, silanol-terminated quartz surface. Finally, the sand was dried at 105 °C and sterilized before each experiment to secure its microbial purity.

Fresh malt spent rootlet feedstock was procured from the Athenian Brewery S.A. (Patras, GR). MSRB was synthesized from pyrolysis at 850 °C for 1 h. More details on the synthesis procedure can be found in Boutsika et al. (2014). The fraction of particles passing through a sieve with an opening of 150 μm was used. The fraction <150 μm had an estimated median particle size $d_{50} \approx$ 75 μm, calculated as the arithmetic mean of the upper sieve opening (150 μm) and the lower limit of detectable fines (~0 μm), assuming an approximately uniform particle size distribution within the sieved fraction; laser diffraction analysis is recommended to refine this estimate in future work. This value was used as a fixed input to the biocolloid transport model (Sect. 3.3), consistent with sieved biochar fractions in similar studies (Suliman et al. 2017). The fraction <150 μm fraction was selected so that the resulting biochar-to-sand median size ratio (≈ 0.15) is small enough to allow adequate dispersion of MSRB within the sand matrix without segregation during dry-packing. Textural properties of the biochar, including surface area, pore volume, and average pore size, were determined via N_2 adsorption–desorption isotherms at 77 K using a TriStar 3000 gas adsorption analyzer (Micromeritics, GA, USA). SSA was calculated using the Brunauer–Emmett–Teller (BET) method.

2.3 Batch sorption and inactivation experiments

Batch sorption experiments were conducted to determine the appropriate kinetic and isotherm models describing *E. coli* adsorption on MSRB. A volume of 10 mL of *E. coli* culture with the desired concentration was transferred into polypropylene tubes containing 10 mg of the sterilized MSRB. Blank samples without the addition of biochar were also prepared in order to estimate bacteria's natural inactivation. All tubes were hooked to a rotor (J.P Selecta, Spain) and rotated at 10 rpm in the dark at room temperature. In every batch experiment, two ionic concentrations of 1 and 150 mM KCl were investigated. The solution with the desired initial bacterial concentration and the adjusted ionic strength was kept for 24 h at 4 °C in order for bacteria to adjust. For the batch experiments, the initial bacterial concentration ranged from 10^2 to 10^7 CFU mL^{-1}. The effect of contact time on *E. coli* sorption was examined for a period of 1 to 48 h. Isotherm experiments were conducted in the same procedure as the kinetic experiments examining the same range of *E. coli* suspensions. Every experiment was conducted in duplicate. The concentrations of Cl^-, PO_4^{3-}, and SO_4^{2-} anions were monitored throughout the batch experiments to ensure that variations that could be attributed to interactions with biochar were minimal (Figure S2a).

2.4 Column transport experiments

A glass chromatography column with a length (L) of 30 cm and an internal diameter (D) of 1 cm (Chromaflex, Kimble Kontes, NJ) was used for the flow-through column transport experiments. Three column configurations were prepared with unamended sand and two mixtures of biochar and sand (namely 5% and 10% w/w MSRB). The biochar-amended sand composite material was thoroughly mixed for 3 h to uniformly distribute the biochar in the sand. The column was dry-packed in the three runs in order to have a more uniform material distribution. The key experimental column parameters are given in Table 1; the resulting porosity values of the 0%, 5%, and 10% w/w MSRB packed columns were 0.335, 0.399, and 0.407, respectively. Column porosity was determined as follows: after dry-packing, the column was saturated from below with degassed DIW at a low flow rate (<0.1 mL min^{-1}) to minimize air entrapment. The pore volume was recorded to those the total volume of water injected until effluent flow reached steady state, and bulk porosity was computed as the ratio of PV to the total column volume ($\pi D^2 L/4 = 23.56\ cm^3$).

The column was placed vertically and operated in an upward mode to displace air from most pores between mixture grains and minimize preferential flow. Before each tracer experiment, sterilized DIW was flushed at a flow rate of 1 mL min^{-1} to wash out the initial high ion concentrations that biochar contains, and to achieve similar water matrix conditions as in batch experiments. The concentrations of Cl^-, PO_4^{3-}, and SO_4^{2-} anions were monitored during the washing period to confirm that adequately low anion concentrations were achieved

Table 1 Experimental parameters for *E. coli* transport in sand-packed columns amended with MSRB

Column	MSRB content (% w/w)	Sand mass (g)	MSRB mass (g)	Porosity ϵ (v/v)	Pore volume PV (mL)	Mixture Bulk density (g cm^{-3})
C1	0	38.890	0.000	0.335	7.90	1.651
C2	5	27.702	1.458	0.399	9.41	1.238
C3	10	24.105	2.675	0.407	9.59	1.137

before initiation of the tracer column experiments (Figure S2b). During the washing period, the Cl^- concentration decreased below the target threshold of 2 mg L^{-1} (i.e., negligible relative to the 1 mM KCl experimental background) after 12–16 PV of DIW flushing, with the range depending on MSRB content. A washing duration corresponding to 15–18 PV was selected as a conservative operational margin to ensure consistent ionic baseline conditions across all column configurations before tracer injection. By conditioning the filter media to a uniform ionic environment, we avoided the introduction of exogenous species, such as Br^-.

Tracer column experiments were conducted with KCl as the conservative tracer to maintain chemical consistency with the batch (1 and 150 mM) experiments. After column washing with 15 to 18 PV of DIW, 4.2 pore volumes of 1 mM KCl were passed at a flow rate (Q) of 1 mL min^{-1}, followed by DIW at the same rate. The 4.2 PV tracer pulse duration was selected to capture the complete conservative tracer breakthrough plateau and the initial elution limb within a single experiment, consistent with standard practice in saturated column transport studies (Bradford et al. 2003; Dan et al. 2021). To facilitate the use of a 1 mM KCl tracer (Cl^- concentration of ≈ 35.5 mg L^{-1}), the effluent Cl^- concentration was reduced to below 2 mg L^{-1} from an initial value of ≈ 46 mg L^{-1} (5% w/w MSRB, C2 column). Effluent samples were collected every 2 min, and Cl^- concentration was measured using ion chromatography (DX-500, Dionex Corp., Sunnyvale, CA). The tracer experiment stopped when the chloride concentration was less than 2 mg L^{-1}.

Before each *E. coli* column transport experiment, 1 mM of KCl solution was passed through the column for 15 h at 0.2 mL min^{-1} to condition the filter media. Each bacterial suspension (≈ $1{\cdot}10^5$ CFU mL^{-1}) was passed into the column at a flow rate (Q) of 1 mL min^{-1} for 4.2 PV. Effluent samples were collected at 2–4 min time intervals and enumerated in microbiological duplicate (two independent spread plates per sample); it should be noted that these are enumeration technical replicates, not independent column replicates. The three column experiments (C1, C2, C3) each represent a single experimental run at their respective MSRB application rates.

2.5 Theory and modelling framework

2.5.1 Bacterial inactivation kinetics

Accurate estimation of *E. coli* inactivation rates is important for decoupling sorption from inactivation in the MSRB batch samples. Several established models were used to study the natural inactivation kinetics of *E. coli* from observations in blank samples. The first-order kinetic model (Bigelow 1921) represents the classical approach to microbial inactivation kinetics. This model assumes that the rate of inactivation is directly proportional to the number of surviving microorganisms at any given time, t, analogous to first-order chemical reactions, yielding the following equation:

$$\ln\frac{C}{C_0} = -k_d t \tag{1}$$

where C_0 (CFU mL^{-1}) is the initial concentration of *E. coli* in the blank samples, C (CFU mL^{-1}) is the surviving *E. coli* concentration at time t, and k_d (min^{-1}) is the first-order inactivation rate constant.

The Weibull model has been widely adopted for modeling microbial inactivation kinetics (Pokhrel et al. 2017; Zhu et al. 2026). It acknowledges biological resistance heterogeneity within microbial populations and derives survival curves from a probability distribution of lethal events, thereby accommodating the non-linear survival curves frequently observed experimentally.

$$\ln\frac{C}{C_0} = -k_d t^{\alpha} \tag{2}$$

where α is a shape factor. For $\alpha = 1$, the Weibull model simplifies to the first-order inactivation model (Eq. 1).

The log-logistic model (Chen and Hoover 2003) represents an alternative mathematical framework where log-time responses follow a logistic (sigmoid) distribution rather than the Weibull distribution. This model emerged from the observation that many microbial inactivation curves exhibit sigmoidal rather than purely monotonic shapes on semi-logarithmic plots with a shoulder and a tail.

$$\log\frac{C}{C_0} = \frac{A}{1+e^{\frac{4\sigma(\tau+6)}{A}}} - \frac{A}{1+e^{\frac{4\sigma(\tau-\log t)}{A}}} \tag{3}$$

where A (log(CFU mL^{-1})) is the difference between upper and lower asymptotes, σ (log(CFU mL^{-1})/log min) is the maximum inactivation rate, and τ (log min) is the log time to maximum inactivation.

The Gompertz function originated in 1825 as a model for human mortality distributions, demonstrating an exponential increase in death rate with age. The modified Gompertz model was adapted for describing bacterial growth curves and later extended to model microbial inactivation kinetics (Acuff et al. 2020; Zwietering et al. 1990). This model was fundamentally designed to accommodate lag phases and asymptotic plateaus.

$$\log\frac{C}{C_0} = Ae^{-e^{BT}} - Ae^{-e^{-B(t-T)}} \tag{4}$$

where T (min) is the time at the maximum inactivation rate, B (min^{-1}) is the relative inactivation rate at $t = T$, and A is as defined previously.

2.5.2 Adsorption kinetics

The kinetics of adsorption of *E. coli* on MSRB were studied using the pseudo-first-order (PFO) and pseudo-second-order (PSO) models with the following generalized differential form:

$$\frac{dq}{dt} = \kappa_m (q_e - q)^m \tag{5}$$

where m is the order of the adsorption model (PFO: $m = 1$; PSO: $m = 2$), q and q_e (CFU mg^{-1}) are the adsorbed *E. coli* concentrations at a given time t and at equilibrium, respectively, and κ_m ((CFU mg^{-1})$^{1-m}$ mL^{-1}) is the m-order adsorption rate constant. Since it is impractical to measure adsorbed *E. coli* concentrations on MSRB, Eq. 5 can be reformulated with regard to the concentration of live *E. coli* in the solution at a given time t by considering the mass balance between aqueous and solid phases and the adopted Weibull *E. coli* inactivation model (due to its superior performance against observations, as demonstrated later in Sect. 3.2):

$$\frac{dC}{dt} = -k_m (C - C_e)^m - \alpha k_d t^{\alpha - 1} C \tag{6}$$

where C_e (CFU mL^{-1}) is the live *E. coli* concentration at equilibrium, $k_m = \kappa_m (M/V)^{1-m}$ ((CFU mL^{-1})$^{1-m}$ min^{-1}), and M/V (mg mL^{-1}) is the adsorbent dosage. For the PFO model, Eq. 6 has the following closed form solution:

$$C(t) = C_0 e^{-k_1 t - k_d t^\alpha} + k_1 C_e \int_0^t e^{k_1(\tau - t) + k_d(\tau^\alpha - t^\alpha)} d\tau \tag{7}$$

whereas for the PSO model, Eq. 6 may be solved numerically.

2.5.3 Adsorption isotherms

To evaluate both the adsorption capacity and the adsorption intensity of *E. coli* on MSRB, the Freundlich model was fitted to the experimental isotherm data, using the equilibrium adsorption values (C_e and q_e) estimated by the PFO kinetic model. Consistent with the SEM analysis presented in the following Sect. 3.1, the Freundlich model was selected to account for the biochar's significant surface heterogeneity and its diverse range of binding sites, because it assumes multilayer sorption on the adsorbent's heterogeneous surface. The Freundlich isotherm model is written as follows:

$$q_e = K_F C_e^{1/n} \tag{8}$$

where K_F ((CFU mg^{-1})/(CFU mL^{-1})$^{1/n}$) and n are constants related to the maximum adsorption capacity and strength of adsorption, respectively.

2.5.4 Transport equations

For each column configuration in Table 1, the dispersivity (λ) was estimated by fitting the one-dimensional advection–dispersion equation (1D-ADE) model to the measured conservative Cl^- tracer effluent data. The 1D-ADE model for a conservative tracer considering that molecular diffusion can be neglected is written as follows:

$$\frac{\partial C}{\partial t} = -U \frac{\partial C}{\partial z} + U\lambda \frac{\partial^2 C}{\partial z^2} \tag{9}$$

where C is the normalized tracer concentration, t (min) is time, z (cm) is the down-gradient distance from the column inlet, U (cm min^{-1}) is the endoporous (or interstitial) velocity (calculated as the superficial velocity divided by the porosity, or $U = 4Q/(\epsilon \pi D^2)$), and λ (cm) is the dispersivity.

The fate and transport of bacteria (and other microorganisms) in saturated porous media are typically described using colloid transport theory, which incorporates the effects of advection, dispersion, retardation, and (reversible) attachment of colloids to a solid surface (Singer et al. 2025). Several studies have pointed out that straining (i.e., the entrapment of colloidal particles within restrictive pore throats and at the interfaces of grain-to-grain junctions) is often overlooked but can be the dominant mechanism of biocolloid retention in sand filtration systems, particularly for fine-textured filter media where the colloid to media size ratio is greater than 0.005 (Bradford et al. 2006). Considering first-order attachment, straining and Weibull *E. coli* inactivation, the generalized form of the one-dimensional biocolloid transport Eq. (1D-BTE) for the live *E. coli* concentration in aqueous and solid phases, C (CFU mL^{-1}) and q (CFU mg^{-1}), respectively, is formulated as follows:

$$R\frac{\partial C}{\partial t} = -U\frac{\partial C}{\partial z} + U\lambda\frac{\partial^2 C}{\partial z^2} - \frac{\rho_b}{\epsilon}\frac{\partial q}{\partial t} - \left(\alpha k_d t^{\alpha-1} + k_{str}\psi_{str}\right)C \tag{10a}$$

$$\frac{\rho_b}{\epsilon}\frac{\partial q}{\partial t} = k_{att}C - k_{det}\frac{\rho_b}{\epsilon}q \tag{10b}$$

where R (-) is the retardation coefficient, ϵ (-) is the media porosity, k_{str} (min^{-1}) is the first-order straining coefficient, ψ_{str} (-) is a dimensionless straining function, k_{att} (min^{-1}) is the first-order attachment coefficient, and k_{det} (min^{-1}) is the first-order detachment coefficient. The

straining function accounts for the depth-dependent entrapment of biocolloids (Bradford et al. 2003):

$$\psi_{str} = \left(\frac{z + d_{50}}{d_{50}}\right)^{-\beta} \tag{11}$$

where β is a shape parameter that controls the biocolloid spatial distribution, and d_{50} (cm) is the median size of the column filter media, which is used as a proxy for the average pore length. Bradford et al. (2003) reported typical values for β between 0.14 and 0.78, with $\beta \approx 0.432$ as a representative value for a wide range of soils. They also reported the following correlation regarding the first-order straining coefficient:

$$k_{str} = 269.7\left(\frac{d_p}{d_{50}}\right)^{1.42} \tag{12}$$

where d_p (cm) is the particle size. Best fit estimates for the retardation (R) and the reversible attachment coefficients (k_{att} and k_{det}) were obtained by fitting Eqs. (10a, b) to the measured *E. coli* effluent data. The parametric 1D-ADE (Eq. 9) and 1D-BTE (Eqs. 10a,b) were solved numerically in Wolfram Mathematica (Wolfram Research Inc. 2026), and model fits were obtained using a non-linear least squares optimization routine.

3 Results and discussion

3.1 Biochar characterization

Based on triplicate measurements, the biochar's SSA and pore volume were determined to be 290 ± 2.9 m^2 g^{-1} and 0.185 ± 0.003 cm^3 g^{-1}, respectively. The *t*-plot method further indicated a significant contribution from microporosity, which represented 63% of the overall pore volume.

The morphological features and surface structure of the biochar were characterized via scanning electron microscopy (SEM), as depicted in Fig. 1. Pyrolysis of MSRB at 850 °C produced a highly fragmented and heterogeneous morphology, characterized by a mix of large, irregular skeletal structures—retaining the original biomass vascular bundles—and finer particulate debris resulting from high-temperature embrittlement. Microscopic analysis revealed a well-developed, honeycomb-like pore network derived from preserved plant cellular walls, which facilitates adsorbate diffusion into the internal matrix. While these carbonaceous walls were relatively thick, they were frequently interspersed with inorganic mineral ash deposits. At higher resolutions, the surface topography was markedly non-uniform, exhibiting a chaotic landscape of jagged ridges, flaky layers, and irregular cavities rather than smooth graphitic planes. This microscale roughness and high density of crevices significantly enhance the biochar's SSA, providing a diverse range of high-energy active sites that contribute to the material's overall adsorption heterogeneity.

The surface chemistry of MSRB at 850 °C is well-characterized in the literature using the same feedstock and pyrolysis protocol (Manariotis et al. 2015). FTIR spectroscopy of MSRB across pyrolysis temperatures of 300–900 °C demonstrated the progressive elimination of all oxygenated functional groups present in raw MSR, including O–H or N–H stretching (~3400 cm^{-1}), aliphatic C–H (~2950 cm^{-1}), and S=O or P=O stretches (~1150 cm^{-1}) corresponding to hydroxyl, phosphonic, amine, and carbon-bonded sulfhydryl groups, with increasing pyrolysis temperature (Manariotis et al. 2015). At 850–900 °C, the spectrum retains only aromatic C=C and C–H bond features, indicating near-complete carbonization and the formation of a predominantly non-polar, graphene-like surface (Manariotis et al. 2015; Keiluweit et al. 2010). The Point of Zero Charge of MSRB at 850 °C was determined as PZC = 8.1, using the pH drift method (50 mg MSRB in 50 mL of 0.01 M KNO_3 solutions pre-adjusted to initial pH 2–11; rotary shaker at 10 rpm, 25 °C, 24 h; PZC identified as the initial pH at which equilibrium pH is unchanged). This value is consistent with the alkaline suspension pH reported by Manariotis et al. (2015) for MSRB at similar pyrolysis

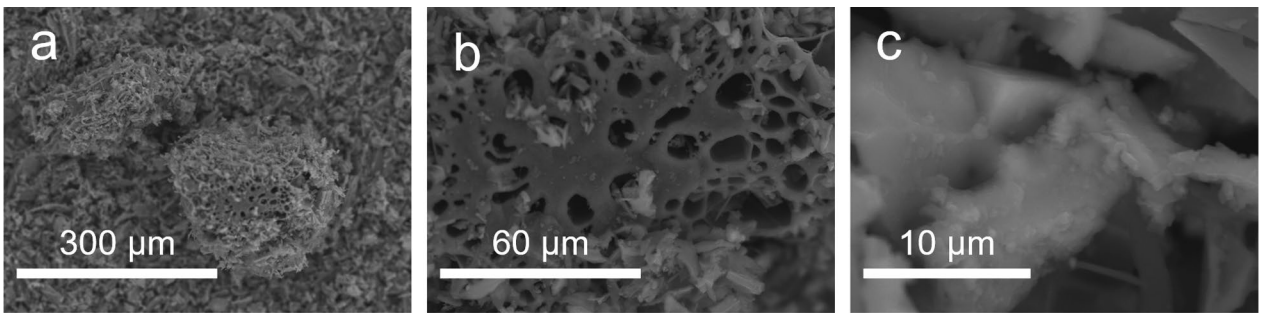

Fig. 1 SEM images of MSRB at **a** 200×, **b** 1000×, and **c** 5000× magnification

temperatures (pH 9.9 at solid loading > 12 g L^{-1}), confirming that at the experimental pH range of this study (6.6–7.6; Table S2), MSRB carried a net positive surface charge (pH < PZC = 8.1). This has important implications for *E. coli* attachment, as demonstrated later in Sect. 3.2.

The potential for MSRB leachate to inhibit *E. coli* viability and thereby confound the inactivation–adsorption distinction was assessed using published data specific to MSRB at 850 °C. Tsouloufa et al. (2020) characterized the physicochemical composition and ecotoxicity of leachates from six serial washes of MSRB produced from the same feedstock (Athenian Brewery S.A., Patras, Greece) at 850 °C under an identical pyrolysis protocol. The first wash aliquot contained elevated concentrations of Cl^- (760 mg L^{-1}), PO_4^{3-} (980 mg L^{-1}), Fe (3380 µg L^{-1}), Zn (1250 µg L^{-1}), and Mn (540 µg L^{-1}); Cd, Pb, Cr, and As were at trace or undetectable levels in all washes. Ecotoxicity testing (Thamnocephalus platyurus; ISO 14380) showed acute toxicity in the 1st wash and slight toxicity in the 2nd, but no acute toxicity was detected from the 3rd wash onward, with the toxic potency strongly correlated with mineral ion load rather than with organic pollutants. In the present study, all columns were flushed with 15–18 pore volumes (PV) of DIW prior to any experiment (Sect. 2.4), a washing intensity substantially exceeding the 3-wash threshold for eliminating acute toxicity identified by Tsouloufa et al. (2020). Effluent Cl^- monitoring confirmed anion concentrations below 2 mg L^{-1} before experiments commenced (Figure S2). We therefore conclude that MSRB leachate would not have exerted any inhibitory effect on *E. coli* under the experimental conditions of this study and does not confound the inactivation–adsorption differentiation in batch experiments.

3.2 Batch experiments

Figure 2 shows the observed survival curves of *E. coli* along with fitted inactivation model curves at the two examined ionic strength conditions. Results showed that higher ionic strength conditions led to an increase in *E. coli* inactivation rates. This is possibly attributed to cell membrane destabilization arising from the increase in the electrochemical gradient between the cytoplasm and the external media (Kuang et al. 2024). To compare the performance of the inactivation models while accounting for differences in the number of parameters, the adjusted coefficient of determination was implemented, defined as $r^2_{adj} = 1 - \left(1 - r^2\right)(N-1)/(N-P-1)$, where N is the total number of observations and P is the total number of model parameters. The first-order model overestimated *E. coli* concentrations during the initial phases and underestimated them at later stages, while the modified Gompertz model exhibited a positive bias at higher times, as it approached its asymptote. The Weibull and log-logistic models produced almost identical results and were the best performers as demonstrated by their higher r^2_{adj} values. In the present study, the Weibull model was selected to model *E. coli* inactivation kinetics due to its combined superior performance and parsimony. Table 2 summarizes the derived parameter values for the Weibull inactivation model, while fitted parameters for the rest of the inactivation models are provided in the Supplementary Information (Table S1).

Figure 3 shows the observed time series of live *E. coli* concentrations in batch experiments, along with

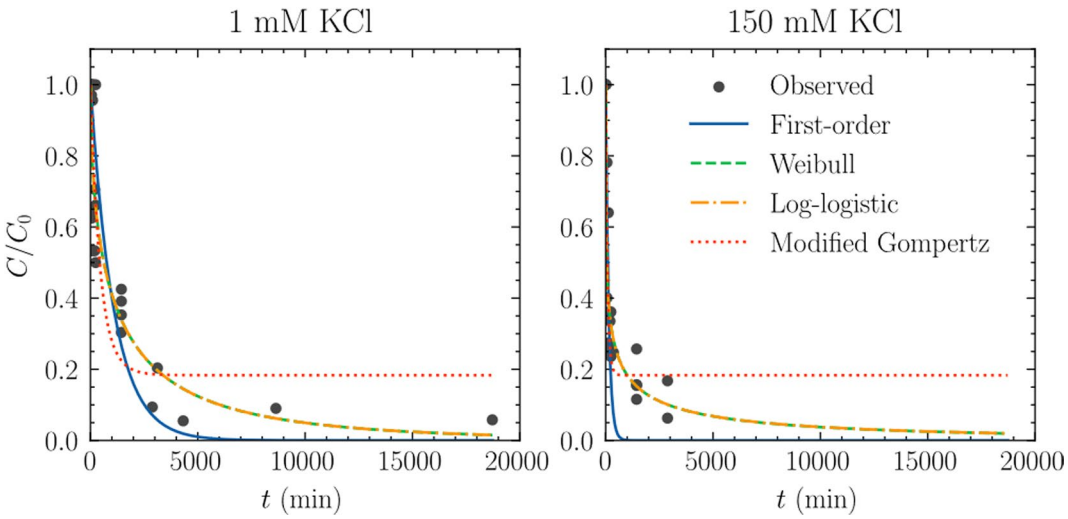

Fig. 2 Comparison of different microbial inactivation models fitted against observed data at two ionic strength conditions

Table 2 Parameter values and adjusted coefficient of determination, r^2_{adj}, of Weibull inactivation model fitted to observed data

Ionic strength [KCl]	$k_d\,(min^{-\alpha})$	α	r^2_{adj}
1 mM	0.02329	0.52778	0.81
150 mM	0.23330	0.28708	0.87

the fitted PFO and PSO models for a wide range of initial concentrations of 10^2–10^7 CFU mL^{-1} and two ionic strengths of 1 and 150 mM KCl. The observed *E. coli* removal efficiency in MSRB batch samples ranged between 77.32% and 99.96% over a period of ~ 3–72 h, reflecting the combined effects of *E. coli* inactivation and sorption on biochar.

The derived kinetic parameters of the PFO and PSO adsorption models and the resulting coefficient of determination are given in Table 3. The conformity between experimental data and model predictions was expressed by the coefficient of determination, r^2. Overall, both kinetic models provided excellent fits, with an average r^2 of 0.91 and 0.95 for PFO and PSO models, respectively. Although the PSO model appears to be statistically superior, the estimated k_2 parameters spanned five orders of magnitude across all runs, in the range of $1.21{\cdot}10^{-9}$–$2.62{\cdot}10^{-4}$ mL (CFU min)$^{-1}$ and were highly correlated with the initial *E. coli* concentration, which might suggest data overfitting. Conversely, the estimated k_1 parameters of the PFO model were relatively consistent across all runs, in the range of $9.70{\cdot}10^{-3}$–$5.92{\cdot}10^{-2}$ min^{-1}. This indicates that the PFO model likely captures the effective rate at which *E. coli* sorption on MSRB approaches equilibrium, which was independent of initial bacterial concentration. Therefore, it may be concluded that sorption of *E. coli* on MSRB followed PFO kinetics.

On average, estimated k_1 values were higher for 1 mM KCl compared to 150 mM KCl ionic strength conditions, possibly suggesting that higher ionic strength hindered adsorption of *E. coli* on MSRB. The observed decrease in k_1 at 150 mM KCl relative to 1 mM KCl is consistent with classical Derjaguin–Landau–Verwey–Overbeek (DLVO) theory. Since MSRB is positively charged (PZC = 8.1 > experimental pH 6.6–7.6) and *E. coli* is negatively charged (Wilson et al. 2001), the interaction between them is governed by electrostatic attraction rather than repulsion. For two oppositely charged surfaces, increasing ionic strength compresses the electrical double layer around both surfaces, reducing the magnitude of their respective surface potentials and thereby attenuating the electrostatic attractive driving force. The reduced adsorption at 150 mM KCl is therefore a direct, DLVO-consistent consequence of double-layer compression weakening the attractive interaction. Direct zeta potential measurements of MSRB and *E. coli* CN-13 under both ionic strength conditions were not conducted in the present study. Such measurements are recommended for future work to provide quantitative support

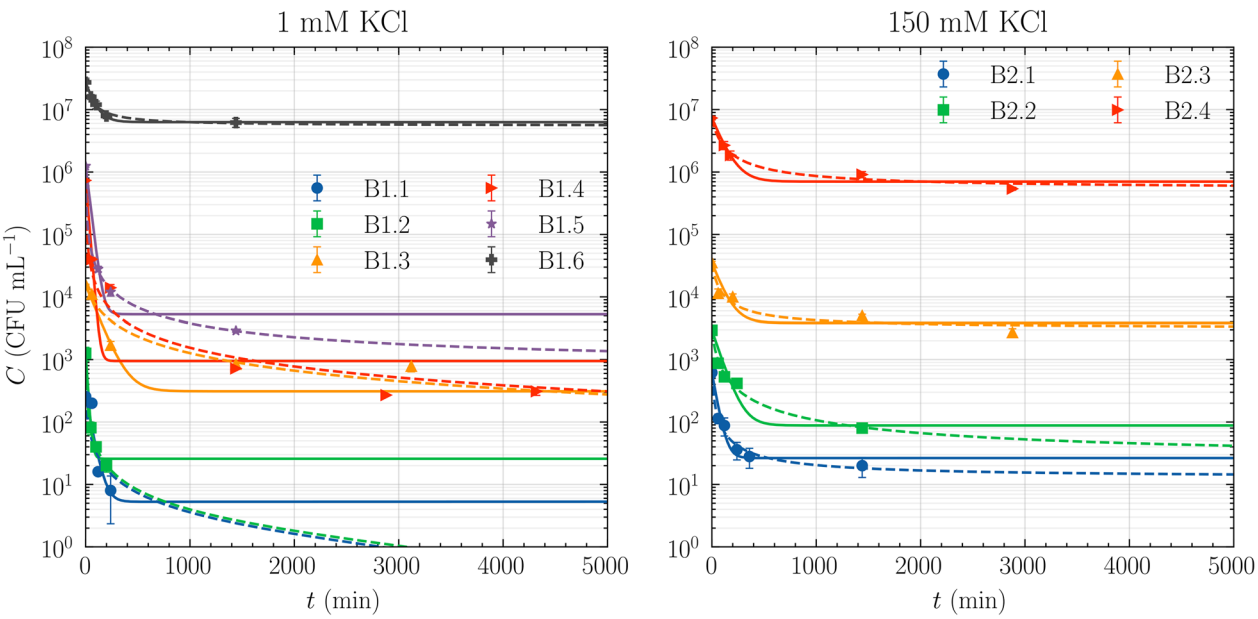

Fig. 3 Live *E. coli* concentration time series in MSRB batch runs at different initial concentrations and at two ionic strength conditions. The points represent measurements, while the solid and dashed lines represent fitted PFO and PSO models, respectively

Table 3 Comparison of PFO and PSO kinetic model parameters for *E. coli* adsorption on MSRB at two ionic strength conditions in batch samples

Run		PFO			PSO		
	C_0 CFU mL^{-1}	C_e CFU mL^{-1}	k_1 min^{-1}	r^2	C_e CFU mL^{-1}	k_2 mL (CFU min)$^{-1}$	r^2
1 mM KCl							
B1.1	$2.56{\cdot}10^{2}$	$5.31{\cdot}10^{0}$	$1.99{\cdot}10^{-2}$	0.89	$3.05{\cdot}10^{-5}$	$2.62{\cdot}10^{-4}$	0.75
B1.2	$1.26{\cdot}10^{3}$	$2.58{\cdot}10^{1}$	$5.92{\cdot}10^{-2}$	0.98	$3.96{\cdot}10^{-4}$	$2.39{\cdot}10^{-4}$	1.00
B1.3	$1.57{\cdot}10^{4}$	$3.11{\cdot}10^{2}$	$9.70{\cdot}10^{-3}$	0.80	$7.52{\cdot}10^{0}$	$7.30{\cdot}10^{-7}$	0.95
B1.4	$7.33{\cdot}10^{5}$	$9.50{\cdot}10^{2}$	$4.71{\cdot}10^{-2}$	0.80	$9.22{\cdot}10^{-3}$	$6.45{\cdot}10^{-7}$	0.98
B1.5	$1.25{\cdot}10^{6}$	$5.28{\cdot}10^{3}$	$3.15{\cdot}10^{-2}$	0.96	$7.61{\cdot}10^{2}$	$3.29{\cdot}10^{-7}$	1.00
B1.6	$2.73{\cdot}10^{7}$	$6.30{\cdot}10^{6}$	$1.35{\cdot}10^{-2}$	1.00	$5.49{\cdot}10^{6}$	$1.21{\cdot}10^{-9}$	0.98
150 mM KCl							
B2.1	$6.19{\cdot}10^{2}$	$2.65{\cdot}10^{1}$	$2.22{\cdot}10^{-2}$	0.95	$1.34{\cdot}10^{1}$	$1.36{\cdot}10^{-4}$	0.98
B2.2	$2.95{\cdot}10^{3}$	$8.81{\cdot}10^{1}$	$1.17{\cdot}10^{-2}$	0.92	$2.52{\cdot}10^{1}$	$1.19{\cdot}10^{-5}$	0.99
B2.3	$3.54{\cdot}10^{4}$	$3.84{\cdot}10^{3}$	$1.08{\cdot}10^{-2}$	0.86	$3.16{\cdot}10^{3}$	$8.94{\cdot}10^{-7}$	0.93
B2.4	$7.33{\cdot}10^{6}$	$7.03{\cdot}10^{5}$	$9.85{\cdot}10^{-3}$	0.97	$5.38{\cdot}10^{5}$	$2.94{\cdot}10^{-9}$	0.98

for this interpretation. As a secondary effect, the high K^+ and Cl^- concentrations at 150 mM may additionally compete for positively charged MSRB surface sites, consistent with observations for chloride–biochar interactions (Azri et al. 2024; Liu et al. 2024).

The results of the surface characterization (Sect. 3.1) allow the adsorption data to be interpreted in terms of the dominant interaction mechanisms between *E. coli* and MSRB. First, regarding the role of micropores: although the *t*-plot analysis indicates that 63% of the total pore volume resides in micropores (< 2 nm diameter), *E. coli* cells (~ 1–2 µm length, ~ 0.5–1 µm diameter) are five orders of magnitude larger than individual micropores and are physically excluded from their interiors. The high micropore volume is nonetheless relevant because it generates the large BET-measured SSA (290 ± 2.9 m^2 g^{-1}), which in conjunction with the rough, fragmented external mesopore and macropore surfaces visible in SEM (Fig. 1) provides abundant high-energy contact sites for bacterial attachment. Second, previous characterization of MSRB by Manariotis et al. (2015) demonstrated that surface functional groups present in the raw material (hydroxyl, phosphonic, amine, carbon-bonded sulfhydryl) progressively disappear with increasing pyrolysis temperature, leaving a predominantly aromatic, highly condensed carbonaceous framework with very low functional group density and a high surface pH (~ 9.9). This implies that *E. coli* attachment to MSRB at 850 °C is governed primarily by hydrophobic and van der Waals interactions between the aromatic graphene-like MSRB surface and the *E. coli* cell envelope, rather than by specific chemical bonding with surface functional groups. The high-temperature MSRB surface is hydrophobic and can facilitate π–π electron donor–acceptor interactions with aromatic moieties in the bacterial lipopolysaccharide outer membrane. This mechanistic interpretation is consistent with the high-temperature biochar literature (Keiluweit et al. 2010).

It is important to emphasize that, since *E. coli* adsorbed onto MSRB cannot be directly enumerated by standard spread-plate methods once cells are associated with the solid phase, the equilibrium concentrations C_e (aqueous phase) and q_e (solid phase) reported in Table 3 are not directly measured quantities. They are model-estimated parameters derived by fitting the closed-form PFO solution (Eq. 7, Sect. 2.5), which embeds the Weibull inactivation correction, to the observed time series of total aqueous-phase *E. coli* concentration. The reliability of these estimates therefore depends on the validity of: (i) the Weibull inactivation model and its parameters (k_d, α from blank experiments); (ii) the PFO kinetic assumption; and (iii) the well-mixed batch reactor assumption. These are inherent limitations of the indirect batch approach for microbiological systems and are shared with published *E. coli*–biochar batch studies (Bolster 2019; Suliman et al. 2017).

The isotherm results and the fitted Freundlich isotherm at two ionic strength conditions are presented in Fig. 4, while the fitted isotherm constants and coefficient of determination are given in Table 4. The high r^2 values demonstrate the effectiveness of the Freundlich model in representing the isotherms of *E. coli* adsorption on MSRB, considering the wide range of concentrations. It should be noted that the Langmuir model failed to fit the experimental isotherm data within

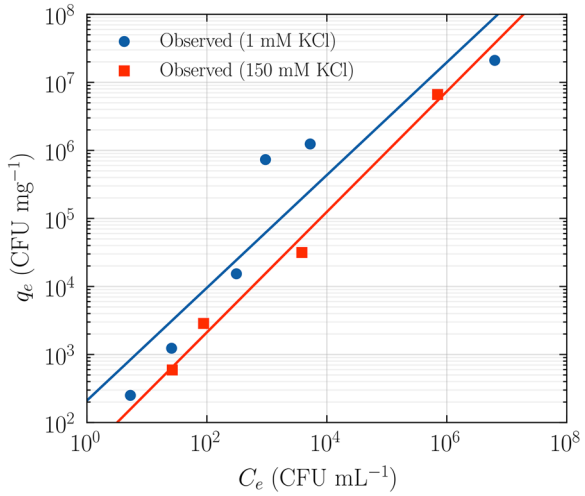

Fig. 4 Observed isotherms of *E. coli* adsorption on MSRB and fitted Freundlich model at two ionic strength conditions

Table 4 Fitted Freundlich isotherm parameters and coefficient of determination at two ionic strength conditions

Ionic strength [KCl]	K_F((CFU mg^{-1})/(CFU mL^{-1})$^{1/n}$)	n	r^2
1 mM	210.512	1.207	0.82
150 mM	35.851	1.129	0.99

physically realistic parameter ranges, likely invalidating the model's inherent assumption of ideal and uniform monolayer sorption on MSRB.

The estimated value of K_F at 1 mM KCl (210.512 (CFU mg^{-1})/(CFU mL^{-1})$^{1/n}$) was higher than its corresponding value at 150 mM KCl (35.851 (CFU mg^{-1})/(CFU mL^{-1})$^{1/n}$), indicating that the adsorption capacity of MSRB exhibited a decline with increasing ionic strength. The estimated value of n at 1 mM KCl (1.207) was slightly higher than its corresponding value at 150 mM KCl (1.129) and both values were slightly greater than unity, suggesting favorable sorption conditions regardless of ionic strength. These results agree with the conclusions drawn in the above adsorption kinetics discussion, demonstrating that lower ionic strength favors the adsorption of *E. coli* on MSRB.

3.3 Column transport experiments

Figure 5 illustrates the observed and simulated effluent concentrations of Cl^- tracer and *E. coli* data, normalized by the initial concentration, for three biochar application rates (C1: 0% w/w MSRB, C2: 5% w/w MSRB, and C3: 10% w/w MSRB). Key fixed model parameters are given in Table S2 for each column configuration. The values of the derived and fitted model parameters, as well as the resulting coefficient of determination of the model fits are given in Table 5, indicating that both models provided excellent fits to the observations ($r^2 > 0.87$).

The column transport experiments demonstrated that amendment of saturated sand with MSRB progressively enhanced *E. coli* retention, achieving removal efficiencies of 17.8% (C1: 0% MSRB), 35.1% (C2: 5% MSRB), and 94.1% (C3: 10% MSRB. These results highlight MSRB's viability as a filtration amendment, with the 10% (w/w)

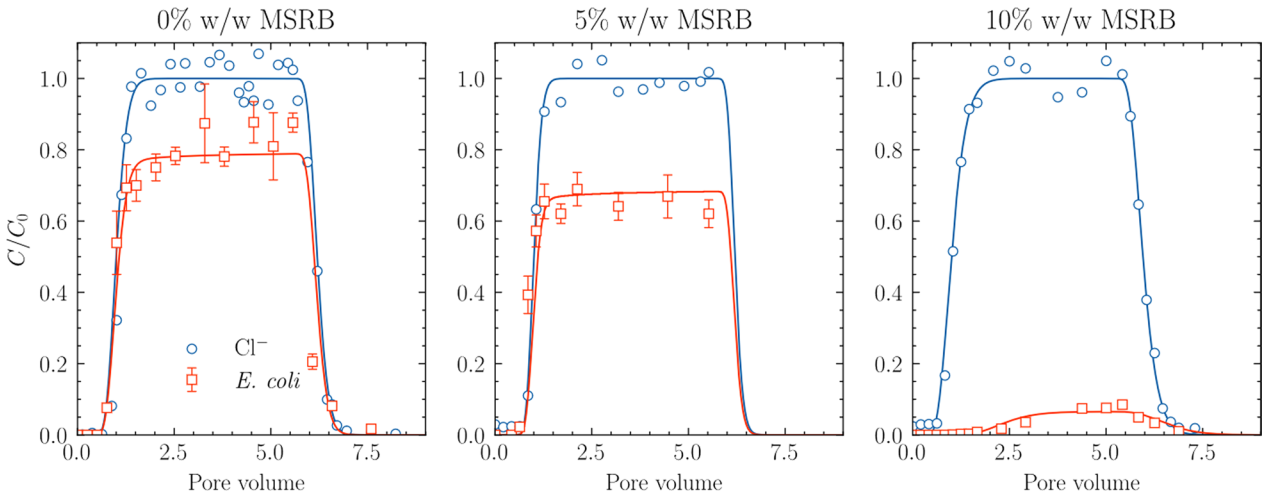

Fig. 5 Normalized effluent Cl^- and *E. coli* concentrations under 3 biochar application rates (0%, 5% and 10% w/w MSRB). Background effluent [KCl] = 1 mM, $C_0 \approx 1{\cdot}10^5$ CFU mL^{-1}, $Q = 1$ mL min^{-1}. Points and solid lines indicate measurements and fitted 1D-ADE and 1D-BTE models, respectively

Table 5 Derived and fitted parameter values of 1D-ADE and 1D-BTE models for three biochar application rates

Column	C1 (0% w/w MSRB)	C2 (5% w/w MSRB)	C3 (10% w/w MSRB)
Derived parameters for 1D-ADE and 1D-BTE models			
U (cm min^{-1})	3.797	3.188	3.128
k_{str} (min^{-1})	0.051	0.076	0.088
Fitted 1D-ADE model parameters using Cl^- tracer data (Eq. 9)			
λ (cm)	0.706	0.373	1.343
r^2	0.976	0.994	0.993
Fitted 1D-BTE model parameters for *E. coli* data (Eqs. 10a,b)			
R	1.000*	1.000*	2.871
k_{att} (min^{-1})	0.022	0.031	0.294
k_{det} (min^{-1})	0.000*	0.000*	0.000*
r^2	0.922	0.873	0.907

*$k_{det} = 0$ and $R = 1.000$ represent boundary values of boundary-constrained optimization

application rate achieving >fivefold greater retention compared to unamended sand conditions.

The 1D-ADE and 1D-BTE models yielded fitted parameters that reveal distinct mechanisms controlling *E. coli* fate and transport in biochar-amended media, by incorporating advection–dispersion, first-order attachment, physical straining, and Weibull inactivation kinetics. The straining coefficient (k_{str}) increased moderately with biochar content, from 0.051 min^{-1} in unamended sand (C1) to 0.088 min^{-1} in the 10% w/w MSRB column (C3), representing a 1.7-fold increase. However, the attachment coefficient (k_{att}) exhibited a dramatically different trend, increasing 13.4-fold from 0.022 min^{-1} in unamended sand to 0.294 min^{-1} in the 10% biochar amendment. Within the 1D-BTE modeling framework, the relative magnitudes of the fitted coefficients suggest that physical straining was the numerically dominant modeled retention pathway at 0% and 5% w/w MSRB, while direct attachment became the dominant modeled mechanism at 10% w/w MSRB. This mechanistic assignment is inherently model-dependent and would require independent spatial profiling of retained bacteria (e.g., column sectioning and enumeration after termination) or pore-scale visualization to confirm experimentally.

Likewise, the retardation coefficient (R) increased substantially only at the highest biochar amendment rate (C3: $R = 2.871$), compared to unity for both unamended sand and the 5% w/w MSRB treatment, indicating that the biochar pore network and particle-size distribution significantly altered the hydrodynamic properties of the porous media at the 10% biochar application rate. These findings align closely with Dan et al. (2021), who reported R values between 1.2 and 4.54 for the transport of phenylurea herbicide in rice straw biochar-amended sand columns. Herein, the observed retardation coefficient trend matches changes in column dispersivity, which decreased from 0.706 cm in unamended sand to 0.373 cm at 5% MSRB but increased to 1.343 cm at 10% MSRB, reflecting the transition from advection-dominated transport in coarse sand to complex flow paths through a mixed grain-size distribution at elevated biochar content. The disproportionate increase in R, λ, and k_{att} relative to k_{str} is likely attributed to the heterogeneous morphology of MSRB, as revealed by SEM analysis (Fig. 1). The MSRB exhibits extensive fragmentation and a honeycomb-like pore network interspersed with mineral ash deposits, creating a complex three-dimensional matrix of pore sizes with continuous tortuous routes that functions as an effective medium for biocolloid retention and substantially alters flow hydrodynamics.

The fitted detachment coefficient k_{det} converged to zero in all three column configurations, which within the 1D-BTE framework is consistent with operationally irreversible *E. coli* attachment under the tested conditions. This finding is supported indirectly by the absence of visible tailing in the effluent breakthrough curves (Fig. 5) during the post-pulse DIW elution phase. It is important to note, however, that $k_{det} = 0$ is a model-fitted boundary-constrained result and should not be interpreted as thermodynamic proof of irreversibility. Mechanistically, the irreversible attachment can be rationalized by the combination of: (i) electrostatic attraction between the positively charged MSRB surface (PZC = 8.1 > experimental pH 6.6–7.6) and negatively charged *E. coli* (Wilson et al. 2001); (ii) hydrophobic interaction between the non-polar, aromatic MSRB surface and the lipid A moiety of the E. coli lipopolysaccharide outer membrane (Manariotis et al. 2015; Keiluweit et al. 2010); and (iii) physical entrapment within surface crevices and pore-throat geometries. These mechanisms collectively create high-energy binding states from which desorption is unfavorable at the experimental pore velocities (3.1–3.8 cm min^{-1}).

This result contrasts with some column transport studies in which partial bacterial breakthrough or "tailing" effects are observed, represented by reversible attachment-detachment equilibria (Bolster 2019; Bradford et al. 2003, 2006; Suliman et al. 2017). The absence of detachment in all three column configurations suggests that either the biochar surface exhibits persistently favorable binding sites with high activation energies for desorption, or the straining mechanism physically isolates entrapped bacteria from the flowing solution, preventing re-entrainment.

4 Conclusions

This study demonstrated the efficacy of MSRB, a readily available brewery industry byproduct, as a sustainable amendment for enhancing the retention of *E. coli* in saturated porous media. The pyrolysis of MSRB at 850 °C produced a carbonaceous material characterized by a high SSA (290 ± 2.9 m^2 g^{-1}) and a heterogeneous, honeycomb-like pore network, which provided abundant active sites for bacterial adsorption.

Batch experiments revealed that the inactivation kinetics of *E. coli* were best described by the Weibull model, which accounted for the non-linear survival curves and biological resistance heterogeneity within the bacterial population. The adsorption kinetics followed the PFO model, indicating that the rate of *E. coli* sorption on MSRB was independent of the initial bacterial concentration. Equilibrium sorption data were well-fitted by the Freundlich isotherm model, consistent with multilayer sorption on a heterogeneous surface. Notably, increasing the ionic strength from 1 to 150 mM KCl resulted in a decrease in the Freundlich affinity coefficient (K_F), suggesting that electrostatic shielding and competitive interactions for binding sites hindered bacterial adsorption under high ionic strength conditions.

Column transport experiments confirmed that MSRB amendment significantly improved the filtration performance of saturated sand. The *E. coli* removal efficiency increased from 17.8% in unamended sand to 94.1% in sand columns amended with 10% (w/w) MSRB. Numerical modeling using the 1D-BTE indicated a shift in the dominant retention mechanism with increasing biochar content. The relative magnitudes of the fitted coefficients suggest that physical straining was the numerically dominant modeled retention pathway at 0% and 5% w/w MSRB, while direct attachment became the dominant modeled mechanism at 10% w/w MSRB, demonstrated by a 13.4-fold increase in the attachment coefficient (k_{att}). Furthermore, the lack of observed detachment ($k_{det} = 0$) across all configurations implied that *E. coli* retention on MSRB was practically irreversible under the tested hydrodynamic conditions.

It is important to note that all experiments were conducted under simplified laboratory conditions that may not fully represent natural field settings. Specifically: (i) sterilized quartz sand and simple KCl background electrolyte were used; natural aquifer and soil matrices contain dissolved organic matter, clay minerals, multivalent cations, and competing colloids that would modify both MSRB surface properties and *E. coli* transport behavior; (ii) a single *E. coli* initial concentration (~ 105 CFU mL^{-1}) and flow rate (1 mL min^{-1}) were tested; (iii) fully saturated upward-flow conditions were imposed, whereas natural vadose zone and soil environments may exhibit unsaturated or preferential flow conditions that reduce filtration efficiency; and (iv) no biofilm, aged or oxidized MSRB, natural organic matter, or competing microorganisms were present. These laboratory-scale findings therefore constitute proof-of-concept evidence, and performance assessment under environmentally representative conditions (including natural water chemistry, competing organic and inorganic matter, unsaturated flow, long-term column operation, and multiple pathogen types) is required before broader field application can be recommended. Furthermore, the column transport results reported here are based on single experimental runs per biochar application rate. Independent column replicates are recommended in future studies to provide formal statistical confidence in the observed removal efficiency differences.

Overall, these findings highlight the potential of MSRB not only as a cost-effective solution for waste management but also as a high-performance amendment for sand filtration systems aimed at mitigating groundwater contamination by pathogenic microorganisms. Future research should assess the long-term performance of MSRB-amended sand filters under variable environmental conditions and in the presence of co-contaminants.

Supplementary Information

The online version contains supplementary material available at https://doi.org/10.1007/s42773-026-00648-2.

Supplementary material 1.

Author contributions

Christos P. Giannopoulos: writing—original draft, data curation, visualization, formal analysis, conceptualization, software. Christos A. Kolotouros: Writing—original draft, investigation—data collection, methodology, data curation, visualization. Ioannis D. Manariotis: Writing—review and editing, conceptualization, supervision, project administration, funding acquisition. All authors read and approved the final manuscript.

Funding

The publication fees of this manuscript have been financed by the Research Council of the University of Patras.

Data availability

The datasets used or analyzed during the current study are available from the corresponding author upon reasonable request.

Declarations

Competing interests

The authors declare that they have no known competing financial interests or personal relationships that could have appeared to influence the work reported in this paper.

Author details

[1]Department of Civil Engineering, Environmental Engineering Laboratory, University of Patras, 26504 Patras, Greece.

Received: 23 January 2026 Revised: 11 May 2026 Accepted: 9 July 2026
Published online: 10 August 2026

References

Abit SM, Bolster CH, Cai P, Walker SL (2012) Influence of feedstock and pyrolysis temperature of biochar amendments on transport of *Escherichia coli* in saturated and unsaturated soil. Environ Sci Technol 46:8097–8105. https://doi.org/10.1021/es300797z

Abit SM, Bolster CH, Cantrell KB et al (2014) Transport of *Escherichia coli*, *Salmonella typhimurium*, and microspheres in biochar-amended soils with different textures. J Environ Qual 43:371–388. https://doi.org/10.2134/jeq2013.06.0236

Acuff JC, Wu J, Marik C et al (2020) Thermal inactivation of *Salmonella*, shiga toxin-producing *Escherichia coli*, *Listeria monocytogenes*, and a surrogate (*Pediococcus acidilactici*) on raisins, apricot halves, and macadamia nuts using vacuum-steam pasteurization. Int J Food Microbiol 333:108814. https://doi.org/10.1016/j.ijfoodmicro.2020.108814

Azri N, Chebbi R, Ouakouak A et al (2024) Single and binary adsorption of paracetamol and diclofenac onto biochar produced from pepper stem: which adsorption properties change in the binary system? Colloids Surf A Physicochem Eng Asp 694:134136. https://doi.org/10.1016/j.colsurfa.2024.134136

Bagordo F, Brigida S, Grassi T et al (2024) Factors influencing microbial contamination of groundwater: a systematic review of field-scale studies. Microorganisms 12:913. https://doi.org/10.3390/microorganisms12050913

Bigelow WD (1921) The logarithmic nature of thermal death time curves. J Infect Dis 29:528–536

Bolster CH (2019) Role of sand size on bacterial retention in biochar-amended sand filters. Biochar 1:353–363. https://doi.org/10.1007/s42773-019-00027-0

Bolster CH, Abit SM (2012) Biochar pyrolyzed at two temperatures affects *Escherichia coli* transport through a sandy soil. J Environ Qual 41:124–133. https://doi.org/10.2134/jeq2011.0207

Boutsika LG, Karapanagioti HK, Manariotis ID (2014) Aqueous mercury sorption by biochar from malt spent rootlets. Water Air Soil Pollut 225:1805. https://doi.org/10.1007/s11270-013-1805-9

Bradford SA, Simunek J, Bettahar M et al (2003) Modeling colloid attachment, straining, and exclusion in saturated porous media. Environ Sci Technol 37:2242–2250. https://doi.org/10.1021/es025899u

Bradford SA, Simunek J, Walker SL (2006) Transport and straining of *E. coli* O157:H7 in saturated porous media. Water Resour Res. https://doi.org/10.1029/2005WR004805

Bui VKH, Nguyen TP, Tran TCP et al (2024) Biochar-based fixed filter columns for water treatment: a comprehensive review. Sci Total Environ 954:176199. https://doi.org/10.1016/j.scitotenv.2024.176199

Chen H, Hoover DG (2003) Modeling the combined effect of high hydrostatic pressure and mild heat on the inactivation kinetics of *Listeria monocytogenes* Scott A in whole milk. Innov Food Sci Emerg Technol 4:25–34. https://doi.org/10.1016/S1466-8564(02)00083-8

Dan Y, Ji M, Tao S et al (2021) Impact of rice straw biochar addition on the sorption and leaching of phenylurea herbicides in saturated sand column. Sci Total Environ 769:144536. https://doi.org/10.1016/j.scitotenv.2020.144536

Downie A, Crosky A, Munroe P (2012) Physical Properties of Biochar. In: Lehmann J, Joseph S (eds) Biochar for Environmental Management. Routledge

García-Ávila F, Galarza-Guamán A, Barros-Bermeo M et al (2023) Integration of high-rate filtration using waste-derived biochar as a potential sustainable technology for drinking water supply. Biochar 5:62. https://doi.org/10.1007/s42773-023-00256-4

Haznedaroglu BZ, Kim HN, Bradford SA, Walker SL (2009) Relative transport behavior of *Escherichia coli* O157:H7 and *Salmonella enterica* serovar pullorum in packed bed column systems: influence of solution chemistry and cell concentration. Environ Sci Technol 43:1838–1844. https://doi.org/10.1021/es802531k

Jha P, Biswas AK, Lakaria BL, Rao AS (2010) Biochar in agriculture – prospects and related implications. Curr Sci 99:1218–1225

Jia X, Zhao X, Zhou Y et al (2023) Tri-functional lanthanum-based biochar for efficient phosphorus recovery, bacterial inhibition, and soil fertility enhancement. Biochar 5:16. https://doi.org/10.1007/s42773-023-00216-y

Kazemi Shariat Panahi H, Dehhaghi M, Ok YS et al (2020) A comprehensive review of engineered biochar: production, characteristics, and environmental applications. J Clean Prod 270:122462. https://doi.org/10.1016/j.jclepro.2020.122462

Keiluweit M, Nico PS, Johnson MG, Kleber M (2010) Dynamic molecular structure of plant biomass-derived black carbon (biochar). Environ Sci Technol 44:1247–1253. https://doi.org/10.1021/es9031419

Korajkic A, McMinn BR, Harwood VJ (2018) Relationships between microbial indicators and pathogens in recreational water settings. Int J Environ Res Public Health 15:2842. https://doi.org/10.3390/ijerph15122842

Kuang J, Lin Y, Wang L et al (2024) Effects of PEF on cell and transcriptomic of *Escherichia coli*. Microorganisms 12:1380. https://doi.org/10.3390/microorganisms12071380

Lehmann J, Gaunt J, Rondon M (2006) Bio-char sequestration in terrestrial ecosystems – a review. Mitig Adapt Strateg Glob Chang 11:403–427. https://doi.org/10.1007/s11027-005-9006-5

Li H, Lin Y, Qin X et al (2024) An updated review on how biochar may possess potential in soil ARGs control on aspects of source, fate and elimination. Biochar 6:24. https://doi.org/10.1007/s42773-024-00319-0

Liu N, Li Y, Zhang M et al (2024) Efficient adsorption of short-chain perfluoroalkyl substances by pristine and Fe/Cu-loaded reed straw biochars. Sci Total Environ 946:174223. https://doi.org/10.1016/j.scitotenv.2024.174223

Manariotis ID, Fotopoulou KN, Karapanagioti HK (2015) Preparation and characterization of biochar sorbents produced from malt spent rootlets. Ind Eng Chem Res 54:9577–9584. https://doi.org/10.1021/acs.iecr.5b02698

Masciopinto C, Fadakar Alghalandis Y (2023) An extended colloid filtration theory for modeling *Escherichia coli* transport in 3-D fracture networks. Water Res 247:120748. https://doi.org/10.1016/j.watres.2023.120748

Mohanty SK, Boehm AB (2014) *Escherichia coli* removal in biochar-augmented biofilter: effect of infiltration rate, initial bacterial concentration, biochar particle size, and presence of compost. Environ Sci Technol 48:11535–11542. https://doi.org/10.1021/es5033162

Pokhrel PR, Bermúdez-Aguirre D, Martínez-Flores HE et al (2017) Combined effect of ultrasound and mild temperatures on the inactivation of *E. coli* in fresh carrot juice and changes on its physicochemical characteristics. J Food Sci 82:2343–2350. https://doi.org/10.1111/1750-3841.13787

Singer MN, Mohsen B, Katzourakis VE et al (2025) Mechanisms governing the transport of nanoparticles and microplastics in porous media: a review. J Environ Chem Eng 13:118002. https://doi.org/10.1016/j.jece.2025.118002

Suliman W, Harsh JB, Fortuna AM et al (2017) Quantitative effects of biochar oxidation and pyrolysis temperature on the transport of pathogenic and nonpathogenic *Escherichia coli* in biochar-amended sand columns. Environ Sci Technol 51:5071–5081. https://doi.org/10.1021/acs.est.6b04535

Tsouloufa A, Dailianis S, Karapanagioti HK, Manariotis ID (2020) Physicochemical and toxicological assay of leachate from malt spent rootlets biochar. Bull Environ Contam Toxicol 104:634–641. https://doi.org/10.1007/s00128-020-02839-4

Wilson WW, Wade MM, Holman SC, Champlin FR (2001) Status of methods for assessing bacterial cell surface charge properties based on zeta potential measurements. J Microbiol Methods 43:153–164. https://doi.org/10.1016/S0167-7012(00)00224-4

Wolf J, Johnston RB, Ambelu A et al (2023) Burden of disease attributable to unsafe drinking water, sanitation, and hygiene in domestic settings: a global analysis for selected adverse health outcomes. Lancet 401:2060–2071. https://doi.org/10.1016/S0140-6736(23)00458-0

Wolfram Research Inc. (2026) Mathematica. https://www.wolfram.com/mathematica. Accessed 12 Jan 2026

Zeng S, Kan E (2023) Enhanced *Escherichia coli* removal from stormwater with bermudagrass-derived activated biochar filtration systems. J Environ Manage 344:118403. https://doi.org/10.1016/j.jenvman.2023.118403

Zhu L, Chattopadhyay S, Elijah Akanbi O et al (2023) Biochar and zero-valent iron sand filtration simultaneously removes contaminants of emerging concern and *Escherichia coli* from wastewater effluent. Biochar 5:41. https://doi.org/10.1007/s42773-023-00240-y

Zhu S, Li B, Chen G (2026) Developing a full Weibull model for microbial survival during food processing. J Food Eng 406:112809. https://doi.org/10.1016/j.jfoodeng.2025.112809

Zwietering MH, Jongenburger I, Rombouts FM, van't Riet K (1990) Modeling of the bacterial growth curve. Appl Environ Microbiol 56:1875–1881. https://doi.org/10.1128/aem.56.6.1875-1881.1990